

1 Electron dynamics in radio frequency magnetron sputtering argon discharges

2 Bocong Zheng,^{1,*} Yangyang Fu,^{2,3,*} Keliang Wang,¹ Thomas Schuelke,^{1,3} and Qi Hua Fan^{1,3,4,†}

3 ¹*Fraunhofer Center for Coatings and Diamond Technologies,
Michigan State University, East Lansing, MI 48824, USA*

4 ²*Department of Computational Mathematics, Science and Engineering,
Michigan State University, East Lansing, MI 48824, USA*

5 ³*Department of Electrical and Computer Engineering,
Michigan State University, East Lansing, MI 48824, USA*

6 ⁴*Department of Chemical Engineering and Materials Science,
Michigan State University, East Lansing, MI 48824, USA*

7 (Dated: October 14, 2020; Email: bzhang@fraunhofer.org [B. Zheng] fuyangya@msu.edu [Y. Fu], qfan@egr.msu.edu [Q. Fan])

8 We demonstrate a self-consistent and complete description of electron dynamics in a typical electropositive
9 radio frequency magnetron sputtering (RFMS) argon discharge. The electron dynamics, including the electron
10 power absorption dynamics in one radio frequency (RF) period, is studied via a fully kinetic 2d3v particle-in-
11 cell/Monte Carlo collision (PIC/MCC) electrostatic simulation. The interplay between the fundamental plasma
12 parameters is analyzed through their spatiotemporal dynamics. The $\mathbf{E} \times \mathbf{B}$ drift-to-discharge current ratio is in
13 approximate agreement with Bohm diffusion. The electron power absorption can be primarily decoupled into the
14 positive Ohmic power absorption in the bulk plasma region and the negative pressure-induced power absorption
15 near the target surface. Ohmic power absorption is the dominant electron power absorption mechanism, mostly
16 contributed by the azimuthal electron current. The power absorption due to electron inertial effects is negligible
17 on time-average. Both the maximum power absorption and dissipation of electrons appear in the bulk plasma
18 region during the second half of the RF period, implying that the nonlocal dynamics of electrons is suppressed
19 in magnetron discharges. The contribution of secondary electrons is negligible under typical RFMS discharge
20 conditions.

12 I. INTRODUCTION

13 Capacitively coupled radio frequency (RF) plasmas are
14 widely used in material processing [1, 2]. Among RF plas-
15 mas, radio frequency magnetron sputtering (RFMS) discharge
16 is one of the most commonly used plasma sources, and has
17 many unique advantages comparing with direct current mag-
18 netron sputtering (DCMS) discharges [3, 4]. In RFMS dis-
19 charges, the target can be selected from a wide variety of ma-
20 terials, including semiconductors and insulators. The mag-
21 netron can maintain a stable discharge and suppress the for-
22 mation of micro-arcs because the charges accumulated on an
23 insulating target surface can be neutralized within one RF pe-
24 riod. Due to the above advantages, RFMS is widely used for
25 fabricating high-quality thin films of various functions, such
26 as transparent conducting films [5–12], photocatalytic thin
27 films [13], piezoelectric thin films [14], solar cells [15], ferro-
28 electric thin films [16–18], nanostructural thin films [19, 20],
29 electroceramic thin films [21], high-entropy alloy films [22],
30 biocompatible thin films [23, 24], and colossal magnetoresis-
31 tance thin films [25]. In physical vapor deposition processes,
32 the properties of deposited thin films depend on the character-
33 istics of the deposition flux [26], such as the ion energy dis-
34 tribution [27–30] and the ion-to-neutral flux ratio [31] of de-
35 posited species at the substrate, which are directly determined
36 by the electron dynamics. This is because the electrons are re-
37 sponsible for the generation of ions via ionization collisions.
38 The generated ions are accelerated by the time-averaged elec-

39 tric field toward the target surface, where they remove target
40 material through sputtering and generate the deposition flux.
41 Therefore, a fundamental knowledge and a thorough under-
42 standing of the electron dynamics in RFMS discharges are of
43 essential significance for controlling and optimizing the dis-
44 charge processes as well as the properties of deposited thin
45 films.

46 In contrast to the wide applications of RFMS discharge, its
47 electron dynamics is still a topic rather poorly understood.
48 Previous studies on the RFMS discharge, including experi-
49 mental diagnoses [27–38] and theoretical analyses [39, 40],
50 have obtained the primary plasma parameters, such as the
51 plasma density, the electron temperature, the ion and elec-
52 tron energy distributions, as well as their spatial and temporal
53 variations. However, due to the complexity of magnetron dis-
54 charges, accurate diagnoses and theoretical studies on electron
55 dynamics under actual geometry and magnetic field distribu-
56 tion are less investigated.

57 In addition to experimental diagnosis and theoretical analy-
58 sis, plasma modeling is also an essential tool in the investiga-
59 tion of magnetron discharges. A simple but commonly used
60 plasma model is the zero-dimensional global model, which
61 has been adopted to study various characteristics of mag-
62 netron discharges [41–54], such as electron heating [43, 46],
63 gas rarefaction [42], self-sputtering [44, 49], target poisoning
64 [48, 50], etc. Albeit the above-mentioned studies are mainly
65 for DCMS, the global model has also been applied in in-
66 vestigating the RFMS discharge [55]. The global model is
67 not computationally expensive. It provides space-averaged
68 plasma parameters and their relationships with process pa-
69 rameters, which helps guide the application of magnetron
70 discharges. Other commonly used models include the fluid
71 model [56–58] and the Monte Carlo model [59]. However,

* These two authors contributed equally to this work.

† Author to whom correspondence should be addressed.

72 these models are self-inconsistent and incomplete; they can-
73 not provide a detailed understanding of the rather complicated
74 RFMS discharge.

75 Particle-in-cell/Monte Carlo collision (PIC/MCC) simula-
76 tion overcomes the above-mentioned disadvantages, and pro-
77 vides a complete and self-consistent picture of magnetron dis-
78 charges [60]. The main disadvantage is the long computation
79 time. PIC simulations have been performed in investigating
80 RFMS discharges for more than two decades [61–70]. The
81 fundamental plasma parameters and their temporal and spatial
82 distributions have been successfully simulated and are consis-
83 tent with experimental results. However, little is known about
84 the electron dynamics of RFMS discharge in a radio frequency
85 period, especially the electron power absorption dynamics.

86 To ionize the background gas, electrons need a certain en-
87 ergy, i.e., the ionization threshold energy of the gas species.
88 Therefore, one of the most fundamental questions in RFMS,
89 as in other RF discharges, is how electrons gain and lose en-
90 ergy. Over the past few decades, this issue has been stud-
91 ied and often referred to as “electron heating” or “electron
92 power absorption”. A considerable amount of work has been
93 reported on the electron power absorption in unmagnetized
94 [71–94] and magnetized [56, 58, 95–106] capacitively cou-
95 pled RF discharges. Through the above investigation, two
96 of the most important electron power absorption mechanisms
97 are identified, i.e., the collisional or Ohmic power absorp-
98 tion due to electron-neutral collisions, and the collisionless or
99 stochastic heating due to momentum transfer from the oscil-
100 lating sheath. Stochastic electron power absorption is gener-
101 ally considered as the dominant power absorption mechanism
102 in low-pressure RF discharges. On the other hand, the domi-
103 nant power absorption mechanism changes from a stochastic
104 to a bulk Ohmic power absorption under a low pressure (e.g.,
105 10 mTorr) if a small transverse magnetic field of 10 G is in-
106 troduced [95, 107]. This enhanced Ohmic power absorption
107 is attributed to the azimuthal electron current, i.e., the $\mathbf{E} \times \mathbf{B}$
108 drift current of electrons [40, 105]. However, this conclusion
109 has not been verified for RFMS discharges in a self-consistent
110 manner and the details are unclear.

111 In this work, we investigate the electron dynamics in RFMS
112 discharges operated in argon at a frequency of 13.56 MHz, a
113 driving voltage of 200 V, and a gas pressure of 10 mTorr via a
114 fully kinetic PIC/MCC simulation. The spatial and temporal
115 dynamics of the fundamental plasma parameters, such as elec-
116 tron densities, electric potentials and fields, as well as electron
117 current densities during one RF period are investigated in de-
118 tail. Animations are provided in the supplementary materials
119 to visually demonstrate the spatiotemporal evolution of these
120 parameters. This paper describes a scenario of electropositive
121 RFMS discharge under typical parameters, including most of
122 the characteristics of electron dynamics under low-pressure
123 magnetized conditions. This paper is structured in the follow-
124 ing way: Section II demonstrates the discharge setup, intro-
125 duces the theoretical background for investigating the electron
126 power absorption based on a moment analysis of the Boltz-
127 mann equation, and describes the PIC/MCC simulation. Sec-
128 tion III illustrates the electron dynamics during one RF period
129 in four subsections: Subsection III A presents the interplay be-

130 tween the electron density and the electric potential and field;
131 Subsection III B discusses the phase difference and the am-
132 plitude ratio of the electron current density in different direc-
133 tions; Subsection III C investigates the different mechanisms
134 of electron power absorption; Subsection III D illustrates the
135 ionization rate and discusses the influence of secondary elec-
136 trons. Finally, conclusions are provided in Section IV.

II. MODELING AND SIMULATION

A. Discharge setup

139 Figure 1(a) illustrates the schematic of a typical planar RF
140 magnetron sputtering set-up. Plasmas are generated between
141 a dielectric target and the upper chamber wall separated by 3
142 cm in the y -direction, with a reflection plane at $x = 0$ cm and
143 confined by the left and right chamber walls. The dielectric
144 target, with a thickness of 0.6 cm and a width of 5.5 cm, is
145 connected to a voltage source which supplies an RF voltage
146 of $V(t) = 200 \cdot \sin(2\pi ft)$ [V], where $f = 1/T = 13.56$ MHz
147 is the driving frequency with T being the RF period. Since
148 the discharge is symmetrical to the central reflection plane,
149 half of the chamber is selected as the simulation region and
150 enclosed by red lines. In the selected simulation region, a bal-
151 anced magnetic field is created by two magnets located under
152 the target, as shown in Fig. 1(b). Due to the magnetic trap,
153 the magnetron plasma is generally nonuniform and concen-
154 trated above the “racetrack” area, where the magnetic field
155 lines are parallel to the target surface and the plasma density
156 is the highest. For this configuration, the maximum parallel
157 magnetic field B_x over the target surface is about 240 G at
158 $x = 2.9$ cm. Other input parameters can be found in Table I.

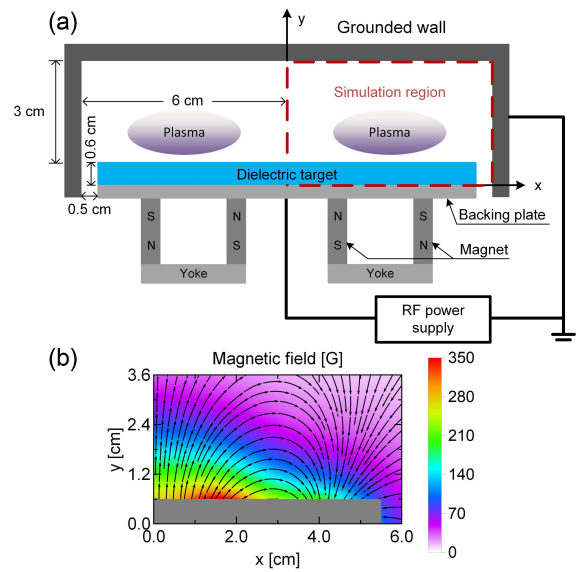


FIG. 1. (a) Schematic of a planar RF magnetron sputtering set-up and (b) the corresponding magnetic field distribution in the simulation region.

TABLE I. The input parameters for the simulation.

Parameter	Value
Gas pressure	10 mTorr
Gas temperature	300 K
Voltage amplitude	200 V
Driving frequency	13.56 MHz
SEE coefficient	0
Electron sticking coefficient	0.5

159

B. Theoretical background

Moment analysis of the Boltzmann equation has been successfully applied in investigating the electron dynamics of one-dimensional unmagnetized [87, 93, 108, 109], magnetized [105, 106], electronegative [106, 110], and two-dimensional unmagnetized [111] capacitively coupled discharges. Here, we use this rigorous analysis to study the electron dynamics of the two-dimensional magnetized RFMS discharge in a self-consistent manner. The magnetized Boltzmann equation for electrons is

$$\frac{\partial f_e}{\partial t} + \mathbf{v} \cdot \nabla f_e - \frac{e}{m_e} (\mathbf{E} + \mathbf{v} \times \mathbf{B}) \cdot \nabla_{\mathbf{v}} f_e = \frac{\partial f_e}{\partial t} \Big|_c, \quad (1)$$

where f_e is the electron distribution function, \mathbf{v} the velocity, m_e and e the electron mass and charge, t the time, \mathbf{E} and \mathbf{B} the electric and magnetic fields. Multiplying the Boltzmann equation by \mathbf{v} and integrating all terms of Eq. (1) over the velocity space, we obtain the momentum conservation equation for electrons

$$m_e n_e \frac{\partial \mathbf{u}_e}{\partial t} + m_e (\Gamma_e \cdot \nabla) \mathbf{u}_e = -e n_e (\mathbf{E} + \mathbf{u}_e \times \mathbf{B}) - \nabla \cdot \overset{\leftrightarrow}{\Pi}_e + \left(\frac{\partial \rho_e}{\partial t} \right)_c, \quad (2)$$

where n_e , \mathbf{u}_e , Γ_e , $\overset{\leftrightarrow}{\Pi}_e$ and $(\partial \rho_e / \partial t)_c$ are the electron density, drift velocity, drift flux, pressure tensor and change of momentum due to collisions, respectively [105]. For the two-dimensional simulation shown in Figure 1, the electric field is in the x - y plane. Hence, the electron power density can be written as

$$P_e(x, y, t) = \mathbf{J}_e \cdot \mathbf{E} = J_{ex} E_x + J_{ey} E_y, \quad (3)$$

where $\mathbf{J}_e = -e n_e \mathbf{u}_e$ is the electron current density in the x - y plane. Multiplying each component of equation (2) in different directions with the corresponding drift velocities, we obtain the electron mechanical energy conservation equations in the x -, y - and z -directions. The sum of these equations gives the total electron mechanical energy conservation equation,

$$P_e = P_{\text{acc}} + P_{\text{in}} + P_{\text{press}} + P_{\text{Ohmic}}, \quad (4)$$

where

$$\begin{aligned} P_{\text{acc}} &= m_e n_e \sum_i u_{ei} \frac{\partial u_{ei}}{\partial t}, \\ P_{\text{in}} &= m_e \sum_i u_{ei} \left(\Gamma_{ex} \frac{\partial u_{ei}}{\partial x} + \Gamma_{ey} \frac{\partial u_{ei}}{\partial y} \right), \\ P_{\text{press}} &= \sum_i u_{ei} \left(\frac{\partial \Pi_{exi}}{\partial x} + \frac{\partial \Pi_{eyi}}{\partial y} \right), \\ P_{\text{Ohmic}} &= - \sum_i u_{ei} \left(\frac{\partial \rho_{ei}}{\partial t} \right)_c, \end{aligned} \quad (5)$$

are the electron power absorption components due to the acceleration term, the inertial term, the pressure-induced effects, and the collisional dynamics. $i = x, y, z$ denotes the axis coordinate. Note that the contribution of Hall fields are eliminated since $\mathbf{u}_e \cdot \mathbf{E}_H = 0$, where the Hall field $\mathbf{E}_H = (-u_{ez} B_y, u_{ez} B_x, u_{ex} B_y - u_{ey} B_x)$.

C. Particle-in-cell/Monte Carlo collision simulation

The two-dimensional simulation is based on our ASTRA PIC/MCC code [105, 112] (see supplementary materials in [105] for the description and the code benchmark with Turner *et al* [113]). As shown in Figure 1, a rectangular magnetron with infinite length is adopted and the magnetron discharge can be described in Cartesian coordinate. The plasma is assumed homogeneous in the “azimuthal” direction and thus the magnetron can be treated in two dimensions. Instability and rotating spokes in the $\mathbf{E} \times \mathbf{B}$ direction, which have been observed in RFMS [114] discharges, may cause the abnormal transport of electrons and ions [115, 116]. However, the frequency of these oscillations is about hundreds of kHz [114], which is two orders of magnitude lower than the radio frequency. The assumption that the plasma is uniform in the azimuthal direction should not affect the general discussion of electron dynamics on the radio frequency time scale.

III. RESULTS

A. Fundamental plasma parameters

In a typical magnetron sputtering discharge, the bulk plasma is highly nonuniform and concentrated above the target surface, where the magnetic field lines are parallel to the target surface and the plasma density is the highest. The target surface in contact with the bulk plasma is often called the “racetrack” area because this area is subjected to the strongest ion bombardment in conventional DCMS, creating a racetrack groove on the target surface. This racetrack area is also the effective target area for collecting current in DCMS, which is generally about one order of magnitude smaller than the total area of the target surface [117, 118]. For RFMS discharges, once the discharge reaches a periodic steady state, the density and profile of the bulk plasma are basically stable, with small changes in one RF period. To investigate the electron

227 dynamics in detail, Figure 2 shows the spatial distributions 266 by the transverse magnetic field and cannot reach the target
 228 of electron density at four typical times during the RF pe- 267 surface. The distortion of the electric potential distribution
 229 riod. The well-confined plasma, with a maximum electron 268 caused by the nonuniform charge accumulation has an impact
 230 density of about $2.2 \times 10^{16}/\text{m}^3$, appears above the target sur- 269 on the electron dynamics, which can be clearly observed from
 231 face at around $x = 2.9$ cm. From Figure 2(b), the electrons 270 the electric field distribution.

232 can only reach the target surface near the phase of $t/T = \pi/2$.

233 At this time, the sinusoidal voltage reaches its positive max-
 234 imum value; the powered electrode temporarily works as an
 235 anode and attracts the electrons. However, the electrons near
 236 the target are magnetized, their motion is restricted by the
 237 transverse magnetic field lines. For the target area right be-
 238 low the bulk plasma region, the magnetic field is basically
 239 parallel to the target surface, which greatly reduces the local
 240 electron flux. Therefore, most of the electrons reach the target
 241 surface at around $x < 1.5$ and $x > 4$ cm, where the magnetic
 242 field lines cross the target surface. This is consistent with pre-
 243 vious simulation results [64]. At $t/T = \pi$ the electrons are no
 244 longer in contact with the target surface and are blown away
 245 at $t/T = 3\pi/2$, when the voltage reaches its negative maxi-
 246 mum value and works as a cathode. For a conductive target,
 247 this nonuniform electron flux to the target surface does not
 248 have much effect on the ion dynamics, because the ions are
 249 not magnetized due to their inertia and only response to the
 250 time-averaged electric field. However, for an insulating target
 251 studied here, the nonuniform electron flux reaching the target
 252 surface results in a nonuniform charge accumulation, which
 253 distorts the electric potential.

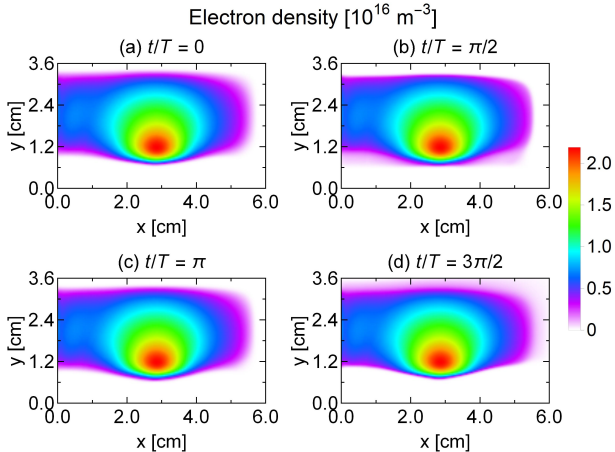


FIG. 2. Electron density at different times during an RF period.

254 Figure 3 shows the electric potential at different times dur-
 255 ing the RF period. Since the powered electrode is insulated 266 by the transverse magnetic field and cannot reach the target
 256 from the plasma by the dielectric target, the DC bias caused 267 surface. The distortion of the electric potential distribution
 257 by the magnetic asymmetric effect [36–38, 119] appears on 268 caused by the nonuniform charge accumulation has an impact
 258 the target surface instead of the electrode. The voltage on the 269 on the electron dynamics, which can be clearly observed from
 259 electrode strictly follows a sinusoidal waveform. The charge 270 the electric field distribution.

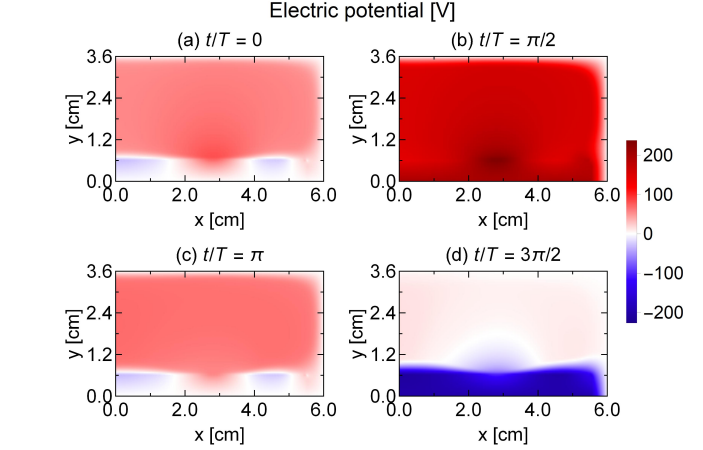


FIG. 3. Electric potential at different times during an RF period.

271 Figure 4 demonstrates the electric field at different times
 272 during the RF period. As shown in Figure 4(b) and (d), when
 273 the electrode voltage is not zero, there is an observable elec-
 274 tric field even in the bulk plasma. This is an obvious differ-
 275 ence from an unmagnetized RF plasma, in which the electric
 276 potential of the bulk plasma is almost constant during an RF
 277 period, and the electric field is close to zero [111]. This elec-
 278 tric potential drop in the bulk plasma region originates from
 279 the confinement of electrons by the magnetic field, which has
 280 been observed in DCMS discharges decades ago [120–123].
 281 In DCMS discharges, the electric potential is funnel-shaped,
 282 similar to Figure 3(d), but generally with a stronger gradient.
 283 This potential profile results in an electric field which accel-
 284 erates ions toward the target surface and forms a racetrack via
 285 sputtering. In RF discharges, ions response to a time-averaged
 286 electric field, which generally points from the bulk plasma re-
 287 gion to the electrodes. Therefore, for RFMS discharges using
 288 a metallic target, the racetrack formed by sputtering is located
 289 on the target surface closest to the bulk plasma region. How-
 290 ever, for RFMS discharges with a dielectric target, the positive
 291 accumulation region on the target surface reduces the local
 292 electric field around $x = 2.9$ cm, where is the racetrack region
 293 in DCMS or RFMS with a metallic target. To sustain the same
 294 ion and electron fluxes at all positions on the dielectric target
 295 surface within one RF period, two electric field peaks appear
 296 at the negative charge accumulation regions. Under this elec-
 297 tric field distribution, the ion flux decreases at around $x = 2.9$
 298 cm and increases on both sides of this area. This may result in
 299 an abnormal erosion profile, that the intensively etched region
 300 on a metallic target can be the least eroded on a dielectric tar-
 301 get, which has been predicted via numerical calculation and
 302 observed in experiments [124].

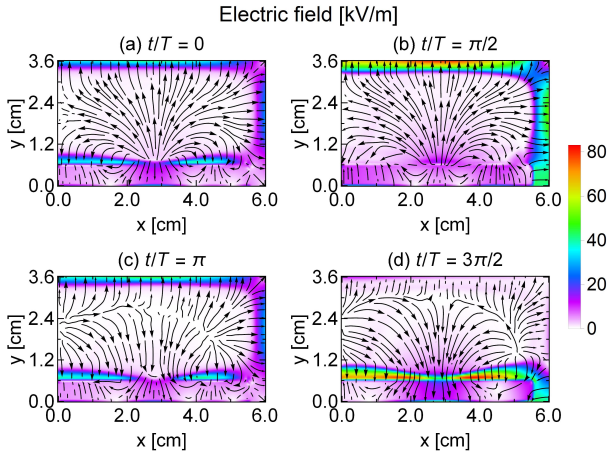


FIG. 4. Electric field at different times during an RF period.

303

B. Electron current densities

304 Figure 5 shows the electron current density at different
 305 times during an RF period. Note that the direction of electron
 306 current is opposite to electron flux since electrons are nega-
 307 tively charged. As shown in Figures 5(a) and (b), during the
 308 first half of the RF period, the electron current flows mainly
 309 from the target to the upper grounded wall, which means that
 310 the electrons are attracted by the positive voltage of the elec-
 311 trode and flow to the target surface. From Figure 4, the elec-
 312 tric field in the negative charge accumulation regions always
 313 points to the target surface, even at $t/T = \pi/2$ when the elec-
 314 trode voltage reaches its positive maximum value. However,
 315 as shown in Figure 5(b), electrons still reach the target surface
 316 at this time due to their inertia. This is the equilibrium state
 317 that the system reaches spontaneously, so that all positions
 318 on the target surface receive the same positive and negative
 319 charges in one RF period. At around $x = 0$ cm, the magnetic
 320 field is basically perpendicular to the target surface; the elec-
 321 tron current changes sinusoidally at a radio frequency of 13.56
 322 MHz along the direction of magnetic field. In the bulk plasma
 323 region, the electron dynamics becomes more complicated un-
 324 der the influence of the magnetic trap. Taking $x = 2.9$ cm
 325 as a symmetry axis, where the plasma density is the highest,
 326 the magnetic field distribution is not exactly symmetrical; as
 327 a result, the electron current direction is slightly inclined to
 328 the upper right, which can be clearly observed in Figures 5(a)
 329 and (c). In the bulk plasma region, the movement of electrons
 330 along the y -direction is constrained by the transverse magnetic
 331 field; the cross-field transport of electrons is facilitated via
 332 collisions with other particles, and through Bohm diffusion
 333 induced by collective effects such as waves and instabilities
 334 [125, 126]. From Figures 5(b) and (d), before the direction
 335 of the electron current changes, the amplitude of the electron
 336 current density along the y -direction, J_{ey} , is greatly reduced;
 337 the electrons at a distance of 1.5–3 cm from the target sur-
 338 face, where the curvature of the magnetic field is relatively
 339 large, can primarily move in the x -direction. However, this
 340 phenomenon only occurs when the direction of the electron

341 current changes. During most of an RF period, the electron
 342 current density along the x -direction, J_{ex} , is about one order of
 343 magnitude lower than J_{ey} , as revealed by previous numerical
 344 investigations [62]. As a result, the contribution of the elec-
 345 tron current in the x -direction to the electron power absorption
 346 is small or even negligible [40], which will be discussed in
 347 Section III C.

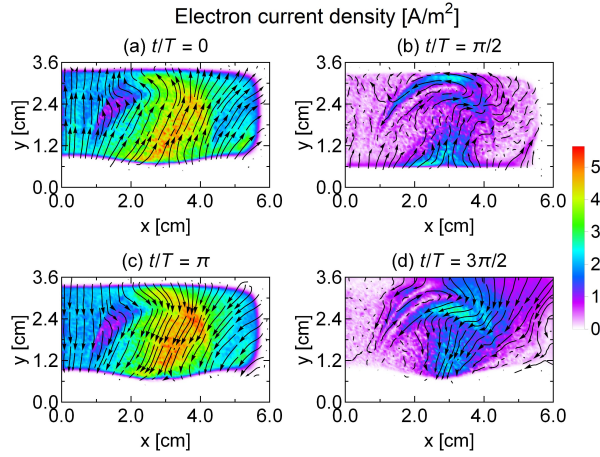


FIG. 5. Electron current density in the x - y plane at different times during an RF period.

348 In magnetron discharges, the azimuthal electron diffusion
 349 along the $\mathbf{E} \times \mathbf{B}$ direction is generally considered to be Bohm
 350 diffusion, i.e., the electron current density along this direction
 351 is dozens of times the discharge current density [127, 128].
 352 This is consistent with what we have observed in RFMS dis-
 353 charges. The azimuthal electron current density along the
 354 $\mathbf{E} \times \mathbf{B}$ direction, J_{ez} , is shown in Figure 6. Note that the unit
 355 of J_{ez} is in kA/m^2 . Since the electrons are negatively charged,
 356 the azimuthal drift direction of electrons is opposite to the di-
 357 rection of J_{ez} , but the same as the $\mathbf{E} \times \mathbf{B}$ direction. During
 358 one RF period, J_{ez} changes sinusoidally at the radio frequency
 359 of 13.56 MHz, with a phase difference to J_{ey} . The phase dif-
 360 ference and amplitude ratio between J_{ez} and J_{ey} are primarily
 361 determined by the electron collision frequency, the electron
 362 cyclotron frequency, and the frequency of the RF source. The
 363 derivation is briefly described as follows.

364 We examine a typical location of $x = 2.9$ cm and $y = 1$ cm,
 365 where the azimuthal electron current density reaches its peak
 366 value. The phase difference and amplitude ratio between J_{ez}
 367 and J_{ey} at the selected location are about 0.28π and 26, respec-
 368 tively. To illustrate the relationship between the phase and the
 369 amplitude of the electron current density in different direc-
 370 tions, in the momentum conservation equation for electrons,
 371 equation (2), neglecting the inertial term $m_e(\boldsymbol{\Gamma}_e \cdot \nabla) \mathbf{u}_e$ and the
 372 pressure term $-\nabla \cdot \overleftrightarrow{\Pi}_e$, using the approximated form of col-
 373 lision term $\left(\frac{\partial p_e}{\partial t}\right)_c = -m_e v_m n_e \mathbf{u}_e$, where v_m is the electron
 374 momentum transfer collision frequency, equation (2) gives

$$m_e n_e \frac{\partial \mathbf{u}_e}{\partial t} = -e n_e (\mathbf{E} + \mathbf{u}_e \times \mathbf{B}) - m_e v_m n_e \mathbf{u}_e. \quad (6)$$

375 Assuming \mathbf{E} and \mathbf{u}_e to be of the form $\exp(-i\omega_{RF}t)$, where

³⁷⁶ $i = \sqrt{-1}$ is the imaginary argument, from equation (6), we
³⁷⁷ have

$$\mathbf{u}_e \times \mathbf{B} = -\mathbf{E} - (v_m - i\omega_{RF})m_e \mathbf{u}_e / e. \quad (7)$$

³⁷⁸ Equation (7) can be further simplified as a tensor equation,

$$\epsilon_0 \omega_{pe}^2 \mathbf{E} = \overset{\leftrightarrow}{\mathbf{A}} \mathbf{J}_e, \quad (8)$$

³⁷⁹ where ϵ_0 is the vacuum permittivity and $\omega_{pe} =$
³⁸⁰ $(e^2 n_e / \epsilon_0 m_e)^{1/2}$ the electron plasma frequency. The ten-
³⁸¹ sor $\overset{\leftrightarrow}{\mathbf{A}}$ is

$$\overset{\leftrightarrow}{\mathbf{A}} = \begin{bmatrix} \xi & \Omega_z & -\Omega_y \\ -\Omega_z & \xi & \Omega_x \\ \Omega_y & -\Omega_x & \xi \end{bmatrix}, \quad (9)$$

³⁸² where $\xi = v_m - i\omega_{RF}$ is a complex frequency, with a real
³⁸³ part from the collision between electrons and neutrals, and an
³⁸⁴ imaginary part from the angular frequency of the RF power
³⁸⁵ supply, $\Omega_x = eB_x/m_e$, $\Omega_y = eB_y/m_e$, and $\Omega_z = eB_z/m_e$ are the
³⁸⁶ electron cyclotron frequencies along different directions. In
³⁸⁷ the selected location of $x = 2.9$ cm and $y = 1$ cm, the mag-
³⁸⁸ netic field along the y -direction can be ignored. In addition,
³⁸⁹ for a two-dimensional model, $B_z = E_z = 0$ is assumed. Using
³⁹⁰ the above simplification, the relationship between the electron
³⁹¹ current density in the y - and z -directions can be obtained from
³⁹² equation (8) as

$$J_{ez} = \frac{\Omega_x}{\xi} J_{ey}. \quad (10)$$

³⁹³ Note that when $\omega_{RF} = 0$, equation (10) degenerates to the
³⁹⁴ classical Hall parameter $J_{ez}/J_{ey} = \Omega_x/v_m$ [127], and is usu-
³⁹⁵ ally written in the form of $\omega_e \tau_{eff}$ [129, 130], where ω_e is the
³⁹⁶ cyclotron angular frequency and τ_{eff} the effective momentum
³⁹⁷ transfer time of electrons. Bohm [125] developed a semiem-
³⁹⁸ pirical diffusion coefficient, $(\omega_e \tau_{eff})_{Bohm} = 16$, which is in
³⁹⁹ close agreement with experimental results, usually within a
⁴⁰⁰ factor of 3. Substituting the calculated frequencies into equa-
⁴⁰¹ tion (10), the phase difference and amplitude ratio between J_{ez}
⁴⁰² and J_{ey} at the selected location is 0.298π and 27.4, close to the
⁴⁰³ above observations of 0.28π and 26. The relationship between
⁴⁰⁴ the electric field and the electron current density can be ob-
⁴⁰⁵ tained as well. Substituting equation (10) into the y -direction
⁴⁰⁶ of equation (8), we have

$$\epsilon_0 \omega_p^2 E_y = \left(\xi + \frac{\Omega_x^2}{\xi} \right) J_{ey}, \quad (11)$$

⁴⁰⁷ the phase difference between E_y and J_{ey} calculated from equa-
⁴⁰⁸ tion (11) is about 0.3π , consistent with the observation in Fig-
⁴⁰⁹ ures 4 and 5. For unmagnetized plasmas $\Omega_x = 0$, equation
⁴¹⁰ (11) gives $J_{ey} = \sigma_p E_y$, where $\sigma_p = \epsilon_0 \omega_{pe}^2 / (v_m - i\omega_{RF})$ is the
⁴¹¹ plasma conductivity. The azimuthal current induces a signif-
⁴¹² icant Ohmic power absorption, which is the primary electron
⁴¹³ power absorption component and will be discussed in Section
⁴¹⁴ III C.

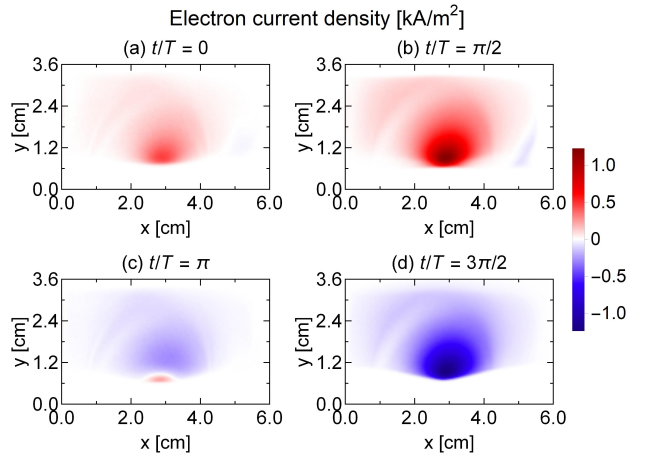


FIG. 6. Azimuthal electron current density at different times during an RF period.

C. Electron power absorption

⁴¹⁵ In RFMS discharges, an RF electric field is applied through
⁴¹⁶ an RF power supply, thereby coupling energy to electrons, in-
⁴¹⁷ ducing ionization, and maintaining a stable discharge. Since
⁴¹⁸ electrons are responsible for generating ions through ioniza-
⁴¹⁹ tion collisions, which bombard the target surface to cause
⁴²⁰ sputtering and particle flux for deposition, one of the most
⁴²¹ fundamental questions in RFMS discharges is how electrons
⁴²² gain and lose energy. Kondo and Nanbu [64] suggested that
⁴²³ the $\mathbf{E} \times \mathbf{B}$ drift and the energy gain via collision with an oscil-
⁴²⁴ lating sheath are the primary electron power absorption mech-
⁴²⁵ anism. Minea and Bretagne [40] provided a simple model
⁴²⁶ for power deposition in RFMS discharges, i.e., by neglecting
⁴²⁷ the inertial and pressure terms in the momentum conserva-
⁴²⁸ tion equation of electrons, the electron power absorption can be
⁴²⁹ shared into the electric field direction and the $\mathbf{E} \times \mathbf{B}$ direc-
⁴³⁰ tion. Albeit the above studies are based on certain assump-
⁴³¹ tions and are not complete, they all capture the main charac-
⁴³² teristics of the electron power absorption in RFMS discharges.
⁴³³ Here we demonstrate a self-consistent and complete descrip-
⁴³⁴ tion of electron power absorption via PIC/MCC simulations
⁴³⁵ and a moment analysis of the Boltzmann equation.

⁴³⁶ By multiplying Figure 4 and Figure 5, we can get the elec-
⁴³⁷ tron power density, $P_e = \mathbf{J}_e \cdot \mathbf{E}$. Figure 7 shows the elec-
⁴³⁸ tron power density P_e at different times during the RF period.
⁴³⁹ The electron power density is primarily comprised of two
⁴⁴⁰ components, i.e., an electron power absorption region in the
⁴⁴¹ bulk plasma region, which is always positive, and an electron
⁴⁴² power absorption region that changes sinusoidally with time
⁴⁴³ in the sheath region. At $t/T = 0$, from Figure 5(a), the elec-
⁴⁴⁴ trons in the bulk plasma region are accelerated by the electric
⁴⁴⁵ field and moving to the target, resulting in a positive P_e ; how-
⁴⁴⁶ ever, as they approaching the target surface, an opposite elec-
⁴⁴⁷ tric field appears in the negative charge accumulation region,
⁴⁴⁸ as shown in Figure 4(a), repels the electrons and results in a
⁴⁴⁹ local negative P_e in Figure 7(a). At $t/T = \pi$, from Figure 5(c),
⁴⁵⁰ the electrons near the target surface and in the bulk plasma re-

gion are repelled and moving away from the target under the corresponding electric field as shown in Figure 4(c); therefore, P_e is positive in both the bulk plasma region and in the sheath. For the same reason, an opposite trend of P_e can be observed near the grounded wall. The most significant electron power absorption occurs at $t/T = \pi/2$ and $t/T = 3\pi/2$; although the electron current densities in the bulk plasma region in Figures 5(b) and (d) are reduced, the considerable electric fields observed in Figures 4(b) and (d), corresponding to the maximum and minimum voltage values, ensure a significant power absorption in the bulk plasma region. For the electron power absorption near the target, P_e is reduced due to the weakened electric field at $t/T = \pi/2$ and the low electron density near the target at $t/T = 3\pi/2$, respectively. The always positive P_e in the bulk plasma region is a typical feature of the Ohmic power absorption, while the time-modulated P_e in the sheath region is a typical feature of the pressure-induced power absorption [87, 93, 105, 111, 131]. In Section II B, a consistent and complete description of the electron power absorption is provided by analyzing the moment of the Boltzmann equation for two-dimensional magnetized plasmas. We use this method to decouple the electron power absorption into different components and study them separately, as described below.

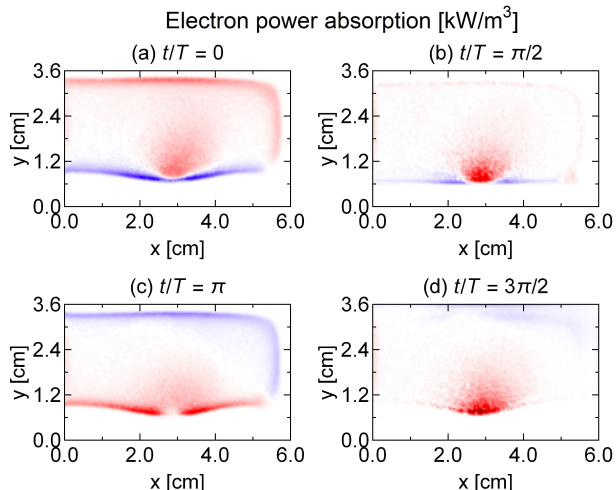


FIG. 7. Electron power density at different times during an RF period.

The time-averaged electron power absorption components are calculated from equations (4) and (5) and the results are illustrated in Figure 8. The first and second terms on the right hand side of equation (4), P_{acc} and P_{in} , are the electron power absorption due to electron inertial effects, which are generally assigned to a collisionless phenomenon. The electron drift velocity \mathbf{u}_e only has a relatively strong temporal and spatial variation in the sheath region, therefore, the contribution of the inertial components is negligible in the bulk plasma region, but can be observed in the sheath region. As shown in Figure 8(a), the acceleration term P_{acc} is positive near the bulk plasma region and negative near the target surface, in the range of about -3.5 – 2.5 kW/m³. The power absorption induced by the time-modulated electron drift velocity is expected to change sinus-

soidally with time; however, since the electrons are attracted and repelled by the target surface within one RF period, the positive and negative power absorption peaks do not overlap in the spatial distribution. The spatiotemporal dynamics of P_{acc} will be shown later. From Figure 8(b), the inertial term P_{in} is mostly positive near the target surface, up to 10 kW/m³. The positive power absorption of P_{in} is primarily contributed from the first half of the RF period, which will be discussed later.

The pressure-induced power absorption P_{press} , as shown in Figure 8(c), is negligible in the bulk plasma region and mostly negative near the target surface. As the dominant power absorption mechanism in low pressure RF discharges [87, 93], P_{press} is also a collisionless mechanism and is related to the concept of “pressure heating” developed by Turner *et al* [72, 74, 78, 95]. However, for magnetized low-pressure RF discharges [95, 105] or RF discharges under very low pressures [132], the dominant mechanism could be the “Ohmic heating”, and the pressure-induced power absorption may even be negative. The last term in equation (4), P_{Ohmic} , is the Ohmic power absorption due to collisions. From Figure 8(d), P_{Ohmic} is the dominant mechanism for RFMS discharge under typical conditions investigated here. This result is similar to the previous one-dimensional PIC/MCC simulation investigation on magnetized RF discharges [105]. Most of the Ohmic power absorption appears in the bulk plasma region, where the azimuthal electron current plays the most important role and the Ohmic power absorption is mostly contributed from the azimuthal direction, since the Ohmic power absorption is proportional to the square of the electron current density in the corresponding direction. The contribution of Ohmic power absorption in x -, y -, and z -directions is 0.6%, 2.1%, and 97.3%, respectively.

Figure 8(e) shows the sum of the above-mentioned power absorption components, $P_{\text{sum}} = P_{\text{acc}} + P_{\text{in}} + P_{\text{press}} + P_{\text{Ohmic}}$. Comparing with Figure 8(f), the power absorption P_{sum} from the sum of each component matches well with the power absorption directly calculated from $\mathbf{J}_e \cdot \mathbf{E}$. The contribution from inertial terms can be neglected and the power absorption can approximately be decoupled as the positive Ohmic power absorption in the bulk plasma region in Figure 8(d), and the negative pressure-induced power absorption near the target surface in Figure 8(c). However, the time-averaged electron power absorption cannot provide the temporal dynamic information; in this respect, the spatiotemporal distribution of power absorption is required.

The temporal dynamics of the electron power absorption at $x = 3$ cm is shown in Figure 9. From Figures 9(a) and (c), the amplitude of P_{acc} in one RF period is up to 190 kW/m³, approximately equivalent to the amplitude of P_{press} . The power absorption from the inertial term, P_{in} , as shown in Figure 9(b), is primarily contributed from the first half of the RF period, when the electrons are attracted to the target surface. The pressure-induced power absorption P_{press} in Figure 9(c) shows a typical spatiotemporal distribution for low pressure RF plasmas. For the Ohmic power absorption, as shown in Figure 9(d), two maximum values appear around $t/T = \pi/2$ and $t/T = 3\pi/2$, where the azimuthal electron current achieves

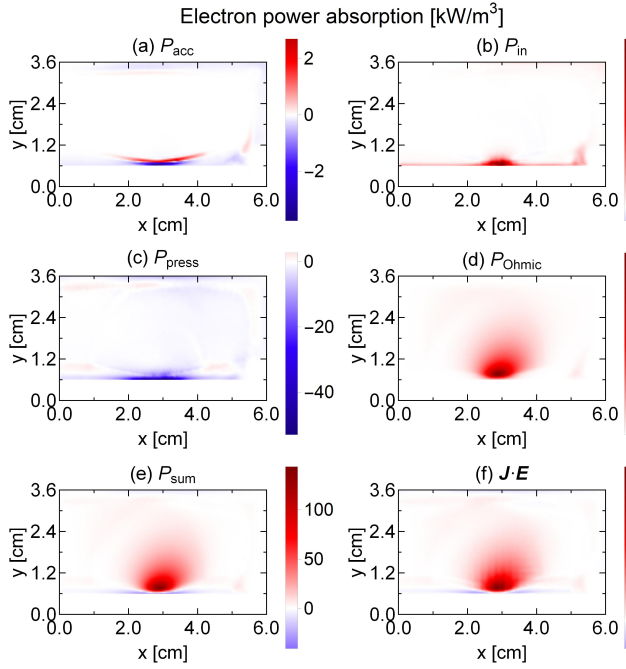


FIG. 8. Spatial distributions of time-averaged electron power absorption components: (a) power absorption due to the acceleration term, P_{acc} ; (b) power absorption due to the inertial term, P_{in} ; (c) power absorption due to pressure-induced effects, P_{press} ; (d) power absorption due to collisional dynamics, P_{Ohmic} ; (e) the sum of the above four power absorption components, P_{sum} ; (f) electron power density calculated from $\mathbf{J}_e \cdot \mathbf{E}$.

location of $x = 2.9$ cm and $y = 1$ cm, $\omega_{\text{RF}}/\Omega_x \approx 0.03$ and $V_m/\Omega_x \approx 0.02$, the Ohmic power absorption ratio between z - and y -directions derived by the analytical model [40] is about $P_{\text{Ohmic}z}/P_{\text{Ohmcy}} \approx 50$, comparable to the contribution of Ohmic power absorption in y - and z -directions directly calculated from the PIC simulation, i.e., 2.1% and 97.3%.

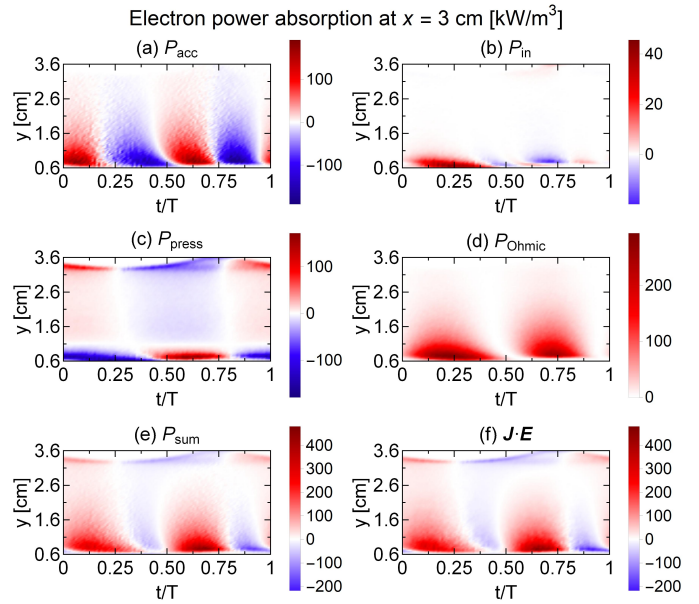


FIG. 9. Temporal dynamics of electron power absorption components at $x = 3$ cm: (a) P_{acc} ; (b) P_{in} ; (c) P_{press} ; (d) P_{Ohmic} ; (e) P_{sum} ; (f) $\mathbf{J}_e \cdot \mathbf{E}$.

its maximum. Comparing Figure 9(e) with Figure 9(f), the spatiotemporal power absorption P_{sum} from the sum of each component is in good agreement with $\mathbf{J}_e \cdot \mathbf{E}$ as well. The spatiotemporal power absorption near the top wall at $y = 3\text{--}3.6$ cm, where the magnetic field is relatively weak (less than 20 G), is primarily contributed by P_{press} ; other components can barely be observed, similar to the unmagnetized case. Due to the strong negative P_{press} near the target surface during the first half of the RF period, the maximum power absorption $\mathbf{J}_e \cdot \mathbf{E}$ appears during the second half of the RF period. The negative $\mathbf{J}_e \cdot \mathbf{E}$ in the bulk plasma region at around $t/T = 0.4$ and $t/T = 0.9$ is contributed from P_{acc} . Comparing this RFMS discharge with a typical low-pressure unmagnetized RF discharge [109], the amplitude of the power absorption induced by inertial effects is significantly increased, which is equivalent to the pressure-induced power absorption; however, the time-averaged contribution is still negligible. Revisiting the study on electron power absorption in RFMS discharges by Minea *et al* [40], their assumptions and conclusions are still correct under the conditions investigated here; by neglecting the inertial and pressure terms, which are not dominant in the bulk plasma region, $\mathbf{J}_e \cdot \mathbf{E}$ can be decomposed into the power absorption in the electric field direction and in the $\mathbf{E} \times \mathbf{B}$ direction. According to their analytical model, the ratio of $P_{\text{Ohmic}z}/P_{\text{Ohmcy}}$ can be derived from the electron momentum transfer collision frequency v_m , the electron cyclotron angular frequency Ω_x , and the RF source frequency ω_{RF} . At the

D. Ionization dynamics

The power absorbed by electrons in the bulk plasma region is dissipated through inelastic collisions, i.e., ionization and excitation for the RFMS discharge simulated here. Figure 10 shows the ionization rate at different times during the RF period, the excitation rate has similar profiles. From the ionization rate profile at different times, ionization occurs mainly in the bulk plasma region, where is therefore often referred to as the “ionization region” [41]. At $t/T = 3\pi/2$, as shown in Figure 10(d), the ionization rate reaches its maximum of up to $1.7 \times 10^{22}/(\text{m}^3 \cdot \text{s})$, when the electrons are repelled from the target and accelerated along the magnetic field lines to the bulk plasma region. Comparing Figures 10 and 7, the power absorption and dissipation of electrons in the bulk plasma region are approximately synchronized in time and space, which is expected in magnetized plasmas. Previous investigations have shown that a magnetic field applied perpendicular to the electric field can suppress the nonlocal electron motion, and collisional bulk electron power absorption becomes dominant [133]. With the increase in the magnetic field, the kinetic property of electrons transition from a nonlocal to a local regime. This is because the magnetic field weakens the electron diffusion in the configuration space but enhances the

603 diffusion in the energy space [134].

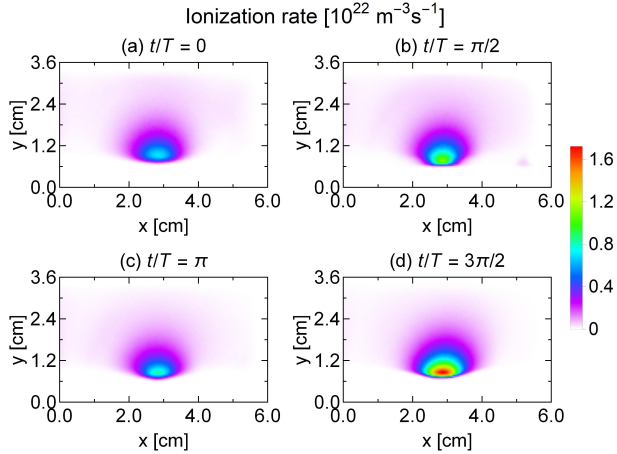


FIG. 10. Ionization rate at different times during an RF period.

604 Secondary electron emission (SEE) induced by positive
605 ions is of essential importance in sustaining the DC magnetron
606 discharges [130, 135]. However, for radio frequency plasmas,
607 especially when the discharge is operated in low-pressure α
608 mode, secondary electrons are not necessary and their contri-
609 bution is negligible. To illustrate the influence of SEE in the
610 RFMS discharge investigated here, an energy-dependent SEE
611 coefficient for argon ions is adopted as [136, 137]:

$$\gamma_i(\varepsilon) = \frac{0.006\varepsilon}{1 + (\varepsilon/10)} + \frac{1.05 \times 10^{-4}(\varepsilon - 80)^{1.2}}{(1 + \varepsilon/8000)^{1.5}}, \quad (12)$$

612 where ε is the argon ion energy. Although this coefficient was
613 originally developed for dirty surfaces, such as oxidized metal
614 surfaces, here we adopt it as an approximation to theoretically
615 investigate the influence of an energy-dependent SEE coeffi-
616 cient in RFMS discharges. With SEE, the RFMS discharge
617 is simulated under the same conditions. Comparing the re-
618 sults with SEE and the above-mentioned results without SEE,
619 there is no observable difference except for the electron en-
620 ergy possibility function (EEPF). For example, the increase in
621 electron density is less than 0.6% (data not shown here). Fig-
622 ure 11 shows the temporal EEPF collected in the entire simu-
623 lation region without and with secondary electrons. Without
624 SEE, as shown in Figure 11(a), the maximum electron energy
625 is around 50 eV, which corresponds to the potential difference
626 between the target surface and the bulk plasma region. With
627 SEE, as shown in Figure 11(b), a high energy tail of up to
628 more than 200 eV appears, corresponding to the maximum po-
629 tential of the RF sheath. This high energy tail comes from the
630 high-energy ballistic electrons (HEBEs) that originate from
631 secondary electrons in low-pressure RF plasmas. However,
632 in a typical low-pressure RFMS discharge, the contribution of
633 secondary electrons to ionization and electron power absorp-
634 tion is negligible, which is consistent with previous studies
635 [62, 64]. This is because the number of ballistic secondary
636 electrons are very small, which was found to be several orders
637 of magnitude less compare to the bulk density. A detailed dis-
638 cussion of HEBEs can be found in [138].

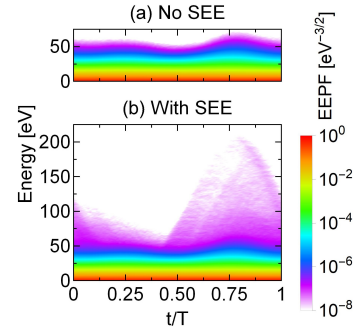


FIG. 11. Temporal EEPF collected in the entire simulation region (a) without and (b) with secondary electrons.

IV. CONCLUSIONS

640 The electron dynamics in a typical electropositive RFMS
641 discharge operated in argon at a frequency of 13.56 MHz, a
642 driving voltage of 200 V, and a gas pressure of 10 mTorr is
643 studied via a fully kinetic, 2d3v PIC/MCC electrostatic sim-
644 ulation. The spatiotemporal dynamics of the fundamental pa-
645 rameters, such as electron densities, electric potentials and
646 fields, as well as electron current densities during one RF pe-
647 riod is demonstrated in detail. The dielectric target commonly
648 used in RFMS discharges accumulates nonuniform charges
649 on its surface, resulting in a reduction in the electric field
650 at the target surface closest to the bulk plasma, and an en-
651 hancement on both sides of the field reduction region. The
652 phase difference and amplitude ratio between electron cur-
653 rent densities in different directions are primarily determined
654 by the electron cyclotron angular frequency, the electron mo-
655 mentum transfer collision frequency, and the RF source fre-
656 quency. The amplitude ratio of the electron current densi-
657 ties in the $\mathbf{E} \times \mathbf{B}$ and the electric field directions, observed in
658 the bulk plasma region, is about 27.4, in approximate agree-
659 ment with the classical Hall parameter in Bohm diffusion. The
660 electron power absorption mechanism is investigated using a
661 self-consistent, spatiotemporal resolved moment analysis of
662 the Boltzmann equation, for which the input parameters are
663 taken from PIC/MCC simulations. In contrast to a variety of
664 previous analyses on electron power absorption in RFMS dis-
665 charges, this method makes no assumptions other than which
666 inherited from PIC simulations, therefore provides a fully self-
667 consistent and complete description of this complicated phe-
668 nomenon. The dominant electron power absorption mech-
669 anism on time- and space-average is the Ohmic power ab-
670 sorption, mostly contributed from the $\mathbf{E} \times \mathbf{B}$ direction. The
671 power absorption due to electron inertial effects is negligi-
672 ble on time-average; therefore, the electron power absorption
673 can be primarily decoupled into the positive power absorp-
674 tion in the bulk plasma region due to collisional dynamics, and
675 the negative power absorption near the target surface due to
676 pressure-induced effects. The ionization rate reaches its max-
677 imum during the second half of the RF period, when the elec-
678 trons are repelled from the target and accelerated to the bulk
679 plasma region. The power absorption and dissipation of elec-

680 trons in the bulk plasma region are approximately synchro- 685
 681 nized in time and space, suggesting a suppression of the non-
 682 local electron motion in magnetron discharges. The contribu-
 683 tion of secondary electrons is negligible under typical RFMS 686
 684 discharge conditions investigated here.

ACKNOWLEDGMENT

This work is partly supported by the National Science Foundation Award Nos. 1917577, 1724941, and 1700787.

-
- 688 [1] M. A. Lieberman and A. J. Lichtenberg, *Principles of plasma 741*
discharges and materials processing (John Wiley & Sons, 742
 New Jersey, 2005). 743
- 689 [2] P. Chabert and N. Braithwaite, *Physics of radio-frequency 744*
plasmas (Cambridge University Press, New York, 2011). 745
- 690 [3] A. Anders, *Journal of Applied Physics* **121**, 171101 (2017). 746
- 691 [4] J. T. Gudmundsson, *Plasma Sources Science and Technology* 747
nil, nil (2020). 748
- 692 [5] K. H. Kim, K. C. Park, and D. Y. Ma, *Journal of Applied 749*
Physics **81**, 7764 (1997). 750
- 693 [6] K.-K. Kim, J.-H. Song, H.-J. Jung, W.-K. Choi, S.-J. Park, 751
 and J.-H. Song, *Journal of Applied Physics* **87**, 3573 (2000). 752
- 694 [7] W. S. Shi, O. Agyeman, and C. N. Xu, *Journal of Applied 753*
Physics **91**, 5640 (2002). 754
- 695 [8] S.-H. Jeong, B.-S. Kim, and B.-T. Lee, *Applied Physics Letters* 755
82, 2625 (2003). 756
- 696 [9] L.-Y. Chen, W.-H. Chen, J.-J. Wang, F. C.-N. Hong, and Y.-K. 757
 Su, *Applied Physics Letters* **85**, 5628 (2004). 758
- 697 [10] C.-C. Lin, S.-Y. Chen, S.-Y. Cheng, and H.-Y. Lee, *Applied 759*
Physics Letters **84**, 5040 (2004). 760
- 698 [11] D.-K. Hwang, H.-S. Kim, J.-H. Lim, J.-Y. Oh, J.-H. Yang, S.-J. 761
 Park, K.-K. Kim, D. C. Look, and Y. S. Park, *Applied Physics 762*
Letters **86**, 151917 (2005). 763
- 699 [12] W.-Y. Chang, Y.-C. Lai, T.-B. Wu, S.-F. Wang, F. Chen, and 764
 M.-J. Tsai, *Applied Physics Letters* **92**, 022110 (2008). 765
- 700 [13] L. Sirghi, *Plasma Sources Science and Technology* **25**, 033003 766
 (2016). 767
- 701 [14] K.-I. Park, S. Xu, Y. Liu, G.-T. Hwang, S.-J. L. Kang, Z. L. 768
 Wang, and K. J. Lee, *Nano Letters* **10**, 4939 (2010). 769
- 702 [15] F. Fu, T. Feurer, T. Jäger, E. Avancini, B. Bissig, S. Yoon, 770
 S. Buecheler, and A. N. Tiwari, *Nature Communications* **6**, 8932 (2015). 771
- 703 [16] C. Yang, M. Chen, T. Hong, C. Wu, J. Wu, and T. Wu, *Applied 772*
Physics Letters **66**, 2643 (1995). 773
- 704 [17] Z. H. Zhou, J. M. Xue, W. Z. Li, J. Wang, H. Zhu, and J. M. 775
 Miao, *Applied Physics Letters* **85**, 804 (2004). 776
- 705 [18] J. Wu and J. Wang, *Acta Materialia* **58**, 1688 (2010). 777
- 706 [19] T. W. Kim, D. U. Lee, and Y. S. Yoon, *Journal of Applied 778*
Physics **88**, 3759 (2000). 779
- 707 [20] W.-J. Li and Z.-W. Fu, *Applied Surface Science* **256**, 2447 780
 (2010). 781
- 708 [21] M. S. Tsai, S. C. Sun, and T. Y. Tseng, *Journal of Applied 782*
Physics **82**, 3482 (1997). 783
- 709 [22] C.-H. Lai, S.-J. Lin, J.-W. Yeh, and S.-Y. Chang, *Surface and 784*
Coatings Technology **201**, 3275 (2006). 785
- 710 [23] V. Nelea, C. Morosanu, M. Iliescu, and I. Mihailescu, *Surface 786*
and Coatings Technology **173**, 315 (2003). 787
- 711 [24] V. Nelea, C. Morosanu, M. Iliescu, and I. Mihailescu, *Applied 788*
Surface Science **228**, 346 (2004). 789
- 712 [25] E. S. Vlakhov, R. A. Chakalov, R. I. Chakalova, K. A. Nenkov, 790
 K. Dörr, A. Handstein, and K.-H. Müller, *Journal of Applied 791*
Physics **83**, 2152 (1998). 792
- 713 [26] A. Anders, *Thin Solid Films* **518**, 4087 (2010). 793
- [27] O. Tsuda, Y. Tatebayashi, Y. Y. Takamura, and T. Yoshida, *Plasma Sources Science and Technology* **8**, 392 (1999).
- [28] D. Gahan, S. Daniels, C. Hayden, P. Scullin, D. O'Sullivan, Y. T. Pei, and M. B. Hopkins, *Plasma Sources Science and Technology* **21**, 024004 (2012).
- [29] S. Bornholdt, J. Ye, S. Ulrich, and H. Kersten, *Journal of Applied Physics* **112**, 123301 (2012).
- [30] S. Bornholdt, N. Itagaki, K. Kuwahara, H. Wulff, M. Shiratani, and H. Kersten, *Plasma Sources Science and Technology* **22**, 025019 (2013).
- [31] S. Ries, L. Banko, M. Hans, D. Primetzhofer, J. M. Schneider, A. Ludwig, P. Awakowicz, and J. Schulze, *Plasma Sources Science and Technology* **28**, 114001 (2019).
- [32] L. I., *Journal of Applied Physics* **58**, 2981 (1985).
- [33] Y. Ohtsu, H. Matsuo, and H. Fujita, *Plasma Sources Science and Technology* **5**, 344 (1996).
- [34] Y. Li, S. Iizuka, and N. Sato, *Plasma Sources Science and Technology* **5**, 241 (1996).
- [35] F. Huang, C. Ye, H. He, Y. Liu, X. Wang, and Z. Ning, *Plasma Sources Science and Technology* **23**, 015003 (2013).
- [36] M. Oberberg, J. Kallähn, P. Awakowicz, and J. Schulze, *Plasma Sources Science and Technology* **27**, 105018 (2018).
- [37] M. Oberberg, D. Engel, B. Berger, C. Wölfel, D. Eremin, J. Lunze, R. P. Brinkmann, P. Awakowicz, and J. Schulze, *Plasma Sources Science and Technology* **28**, 115021 (2019).
- [38] M. Oberberg, B. Berger, M. Buschheuer, D. Engel, C. Wölfel, D. Eremin, J. Lunze, R. P. Brinkmann, P. Awakowicz, and J. Schulze, *Plasma Sources Science and Technology* **29**, 075013 (2020).
- [39] M. Lieberman, A. Lichtenberg, and S. Savas, *IEEE Transactions on Plasma Science* **19**, 189 (1991).
- [40] T. M. Minea and J. Bretagne, *Plasma Sources Science and Technology* **12**, 97 (2003).
- [41] M. A. Raadu, I. Axnäs, J. T. Gudmundsson, C. Huo, and N. Brenning, *Plasma Sources Science and Technology* **20**, 065007 (2011).
- [42] C. Huo, M. A. Raadu, D. Lundin, J. T. Gudmundsson, A. Anders, and N. Brenning, *Plasma Sources Science and Technology* **21**, 045004 (2012).
- [43] C. Huo, D. Lundin, M. A. Raadu, A. Anders, J. T. Gudmundsson, and N. Brenning, *Plasma Sources Science and Technology* **22**, 045005 (2013).
- [44] C. Huo, D. Lundin, M. A. Raadu, A. Anders, J. T. Gudmundsson, and N. Brenning, *Plasma Sources Science and Technology* **23**, 025017 (2014).
- [45] B. C. Zheng, D. Meng, H. L. Che, and M. K. Lei, *Journal of Applied Physics* **117**, 203302 (2015).
- [46] N. Brenning, J. T. Gudmundsson, D. Lundin, T. Minea, M. A. Raadu, and U. Helmersson, *Plasma Sources Science and Technology* **25**, 065024 (2016).
- [47] C. Huo, D. Lundin, J. T. Gudmundsson, M. A. Raadu, J. W. Bradley, and N. Brenning, *Journal of Physics D: Applied Physics* **50**, 354003 (2017).

- [48] B. C. Zheng, Z. L. Wu, B. Wu, Y. G. Li, and M. K. Lei, *Journal of Applied Physics* **121**, 171901 (2017).
- [49] N. Brenning, J. T. Gudmundsson, M. A. Raadu, T. J. Petty, T. Minea, and D. Lundin, *Plasma Sources Science and Technology* **26**, 125003 (2017).
- [50] D. Lundin, J. T. Gudmundsson, N. Brenning, M. A. Raadu, and T. M. Minea, *Journal of Applied Physics* **121**, 171917 (2017).
- [51] B. Zheng, Z. Wu, S. Cui, S. Xiao, L. Liu, H. Lin, R. K. Y. Fu, X. Tian, F. Pan, and P. K. Chu, *IEEE Transactions on Plasma Science* **47**, 193 (2019).
- [52] S. Cui, Z. Wu, H. Lin, S. Xiao, B. Zheng, L. Liu, X. An, R. K. Y. Fu, X. Tian, W. Tan, and P. K. Chu, *Journal of Applied Physics* **125**, 063302 (2019).
- [53] S. Cui, Z. Wu, S. Xiao, B. Zheng, L. Chen, T. Li, R. K. Y. Fu, P. K. Chu, X. Tian, W. Tan, D. Fang, and F. Pan, *Journal of Applied Physics* **127**, 023301 (2020).
- [54] L. Chen, S. Cui, W. Tang, L. Zhou, T. Li, L. Liu, X. An, Z. Wu, Z. Ma, H. Lin, X. Tian, R. K. Fu, P. K. Chu, and Z. Wu, *Plasma Sources Science and Technology* **29**, 025016 (2020).
- [55] L. Maaloul, S. Morel, and L. Stafford, *Journal of Vacuum Science & Technology A: Vacuum, Surfaces, and Films* **30**, 021301 (2012).
- [56] M. J. Kushner, *Journal of Applied Physics* **94**, 1436 (2003).
- [57] S. Rauf, *Plasma Sources Science and Technology* **14**, 329 (2005).
- [58] Y. Yang and M. J. Kushner, *Journal of Vacuum Science & Technology A: Vacuum, Surfaces, and Films* **25**, 1420 (2007).
- [59] E. Bultinck and A. Bogaerts, *Plasma Sources Science and Technology* **20**, 045013 (2011).
- [60] A. Bogaerts, E. Bultinck, I. Kolev, L. Schwaederlé, K. V. Aeken, G. Buyle, and D. Depla, *Journal of Physics D: Applied Physics* **42**, 194018 (2009).
- [61] T. Minea, J. Bretagne, and G. Gousset, *IEEE Transactions on Plasma Science* **27**, 94 (1999).
- [62] T. Minea, J. Bretagne, G. Gousset, L. Magne, D. Pagnon, and M. Touzeau, *Surface and Coatings Technology* **116-119**, 558 (1999).
- [63] T. M. Minea, J. Bretagne, D. Pagnon, and M. Touzeau, *Journal of Physics D: Applied Physics* **33**, 1884 (2000).
- [64] S. Kondo and K. Nanbu, *Journal of Vacuum Science & Technology A: Vacuum, Surfaces, and Films* **19**, 838 (2001).
- [65] J. Bretagne, C. B. Laporte, G. Gousset, O. Leroy, T. M. Minea, D. Pagnon, L. de Poucques, and M. Touzeau, *Plasma Sources Science and Technology* **12**, S33 (2003).
- [66] S. Yonemura and K. Nanbu, *IEEE Transactions on Plasma Science* **31**, 479 (2003).
- [67] S. Yonemura and K. Nanbu, *IEEE Transactions on Plasma Science* **33**, 350 (2005).
- [68] S. Yonemura and K. Nanbu, *Thin Solid Films* **506-507**, 517 (2006).
- [69] D. Benyoucef and M. Yousfi, *IEEE Transactions on Plasma Science* **41**, 829 (2013).
- [70] D. Benyoucef and M. Yousfi, *Plasma Sources Science and Technology* **23**, 044007 (2014).
- [71] V. A. Godyak and R. B. Piejak, *Physical Review Letters* **65**, 996 (1990).
- [72] M. M. Turner, *Physical Review Letters* **75**, 1312 (1995).
- [73] M. Lieberman and V. Godyak, *IEEE Transactions on Plasma Science* **26**, 955 (1998).
- [74] G. Gozadinos, M. M. Turner, and D. Vender, *Physical Review Letters* **87**, 135004 (2001).
- [75] S. J. You, S. K. Ahn, and H. Y. Chang, *Applied Physics Letters* **89**, 171502 (2006).
- [76] T. Mussenbrock and R. P. Brinkmann, *Applied Physics Letters* **88**, 151503 (2006).
- [77] T. Mussenbrock, R. P. Brinkmann, M. A. Lieberman, A. J. Lichtenberg, and E. Kawamura, *Physical Review Letters* **101**, 085004 (2008).
- [78] M. M. Turner, *Journal of Physics D: Applied Physics* **42**, 194008 (2009).
- [79] Y.-X. Liu, Q.-Z. Zhang, W. Jiang, L.-J. Hou, X.-Z. Jiang, W.-Q. Lu, and Y.-N. Wang, *Physical Review Letters* **107**, 055002 (2011).
- [80] Z. Donkó, J. Schulze, U. Czarnetzki, A. Derzsi, P. Hartmann, I. Korolov, and E. Schüngel, *Plasma Physics and Controlled Fusion* **54**, 124003 (2012).
- [81] T. Lafleur, P. A. Delattre, E. V. Johnson, and J. P. Booth, *Applied Physics Letters* **101**, 124104 (2012).
- [82] T. Lafleur, R. W. Boswell, and J. P. Booth, *Applied Physics Letters* **100**, 194101 (2012).
- [83] T. Lafleur and R. W. Boswell, *Physics of Plasmas* **19**, 023508 (2012).
- [84] T. Lafleur, P. Chabert, M. M. Turner, and J. P. Booth, *Physics of Plasmas* **20**, 124503 (2013).
- [85] J. Schulze, Z. Donkó, A. Derzsi, I. Korolov, and E. Schuengel, *Plasma Sources Science and Technology* **24**, 015019 (2014).
- [86] T. Lafleur, P. Chabert, M. M. Turner, and J. P. Booth, *Plasma Sources Science and Technology* **23**, 015016 (2014).
- [87] T. Lafleur, P. Chabert, and J. P. Booth, *Plasma Sources Science and Technology* **23**, 035010 (2014).
- [88] T. Lafleur and P. Chabert, *Plasma Sources Science and Technology* **24**, 044002 (2015).
- [89] R. P. Brinkmann, *Plasma Sources Science and Technology* **25**, 014001 (2015).
- [90] J. Schulze and T. Mussenbrock, *Plasma Sources Science and Technology* **25**, 020401 (2016).
- [91] J. T. Gudmundsson and D. I. Snorrason, *Journal of Applied Physics* **122**, 193302 (2017).
- [92] J. T. Gudmundsson, D. I. Snorrason, and H. Hannesdottir, *Plasma Sources Science and Technology* **27**, 025009 (2018).
- [93] J. Schulze, Z. Donkó, T. Lafleur, S. Wilczek, and R. P. Brinkmann, *Plasma Sources Science and Technology* **27**, 055010 (2018).
- [94] S. Rauf, *Plasma Sources Science and Technology* **nil**, nil (2020).
- [95] M. M. Turner, D. A. W. Hutchinson, R. A. Doyle, and M. B. Hopkins, *Physical Review Letters* **76**, 2069 (1996).
- [96] J.-C. Park and B. Kang, *IEEE Transactions on Plasma Science* **25**, 499 (1997).
- [97] S. J. You, C. W. Chung, K. H. Bai, and H. Y. Chang, *Applied Physics Letters* **81**, 2529 (2002).
- [98] S. H. Lee, S. J. You, H. Y. Chang, and J. K. Lee, *Journal of Vacuum Science & Technology A: Vacuum, Surfaces, and Films* **25**, 455 (2007).
- [99] S. J. You, G. Y. Park, J. H. Kwon, J. H. Kim, H. Y. Chang, J. K. Lee, D. J. Seong, and Y. H. Shin, *Applied Physics Letters* **96**, 101504 (2010).
- [100] S. You, T. Hai, M. Park, D. Kim, J. Kim, D. Seong, Y. Shin, S. Lee, G. Park, J. Lee, and H. Chang, *Thin Solid Films* **519**, 6981 (2011).
- [101] Y. Ohtsu and T. Yanagise, *Plasma Sources Science and Technology* **24**, 034005 (2015).
- [102] S. Dujko, D. Bošnjaković, R. D. White, and Z. L. Petrović, *Plasma Sources Science and Technology* **24**, 054006 (2015).
- [103] S. Yang, M. E. Innocenti, Y. Zhang, L. Yi, and W. Jiang, *Journal of Vacuum Science & Technology A: Vacuum, Surfaces, and Films* **35**, 061311 (2017).

- 922 [104] S. Binwal, J. K. Joshi, S. K. Karkari, P. K. Kaw, and L. Nair, *Journal of Vacuum Science & Technology B: Microelectronics and Nanometer Structures* **23**, 2218 (2005).
- 923 [105] B. Zheng, K. Wang, T. Grotjohn, T. Schuelke, and Q. H. Fan, *Plasma Sources Science and Technology* **28**, 09LT03 (2019).
- 924 [106] L. Wang, D.-Q. Wen, P. Hartmann, Z. Donko, A. Derzsi, X. W. Wang, Y.-H. Song, Y.-N. Wang, and J. Schulze, *Plasma Sources Science and Technology* **29**, nil (2020).
- 925 [107] D. Hutchinson, M. Turner, R. Doyle, and M. Hopkins, *IEEE Transactions on Plasma Science* **23**, 636 (1995).
- 926 [108] M. Surendra and M. Dalvie, *Physical Review E* **48**, 3914 (1993).
- 927 [109] S. Wilczek, J. Schulze, R. P. Brinkmann, Z. Donkó, J. Trieschmann, and T. Mussenbrock, *Journal of Applied Physics* **127**, 181101 (2020).
- 928 [110] A. Proto and J. T. Gudmundsson, *Journal of Applied Physics* **128**, 113302 (2020).
- 929 [111] Y. Liu, J.-P. Booth, and P. Chabert, *Plasma Sources Science and Technology* **27**, 025006 (2018).
- 930 [112] B. Zheng, Y. Fu, D. qi Wen, K. Wang, T. Schuelke, and Q. H. Fan, *Journal of Physics D: Applied Physics* **53**, 435201 (2020).
- 931 [113] M. M. Turner, A. Derzsi, Z. Donkó, D. Eremin, S. J. Kelly, T. Lafleur, and T. Mussenbrock, *Physics of Plasmas* **20**, 013507 (2013).
- 932 [114] M. Panjan, *Journal of Applied Physics* **125**, 203303 (2019).
- 933 [115] M. Panjan, R. Franz, and A. Anders, *Plasma Sources Science and Technology* **23**, 025007 (2014).
- 934 [116] R. Franz, C. Clavero, J. Kolbeck, and A. Anders, *Plasma Sources Science and Technology* **25**, 015022 (2016).
- 935 [117] A. Anders and E. Oks, *Journal of Applied Physics* **106**, 023306 (2009).
- 936 [118] A. Anders, *Surface and Coatings Technology* **204**, 2864 (2010).
- 937 [119] S. Yang, L. Chang, Y. Zhang, and W. Jiang, *Plasma Sources Science and Technology* **27**, 035008 (2018).
- 938 [120] J. W. Bradley, S. Thompson, and Y. A. Gonzalvo, *Plasma Sources Science and Technology* **10**, 490 (2001).
- 939 [121] A. Mishra, P. J. Kelly, and J. W. Bradley, *Plasma Sources Science and Technology* **19**, 045014 (2010).
- 940 [122] A. Mishra, P. J. Kelly, and J. W. Bradley, *Journal of Physics D: Applied Physics* **44**, 425201 (2011).
- 941 [123] A. Rauch, R. J. Mendelsberg, J. M. Sanders, and A. Anders, *Journal of Applied Physics* **111**, 083302 (2012).
- 942 [124] S. Kuroiwa, T. Mine, T. Yagisawa, and T. Makabe, *Journal of Vacuum Science & Technology B: Microelectronics and Nanometer Structures* **23**, 2218 (2005).
- 943 [125] D. Bohm, Qualitative Description of the Arc Plasma in a Magnetic Field (1949).
- 944 [126] F. Chen, *Introduction to Plasma Physics and Controlled Fusion* (Springer International Publishing, Switzerland, 2016).
- 945 [127] S. M. Rossnagel and H. R. Kaufman, *Journal of Vacuum Science & Technology A: Vacuum, Surfaces, and Films* **5**, 88 (1987).
- 946 [128] S. M. Rossnagel and H. R. Kaufman, *Journal of Vacuum Science & Technology A: Vacuum, Surfaces, and Films* **5**, 2276 (1987).
- 947 [129] N. Brenning, R. L. Merlino, D. Lundin, M. A. Raadu, and U. Helmersson, *Physical Review Letters* **103**, 225003 (2009).
- 948 [130] J. T. Gudmundsson, N. Brenning, D. Lundin, and U. Helmersson, *Journal of Vacuum Science & Technology A: Vacuum, Surfaces, and Films* **30**, 030801 (2012).
- 949 [131] M. Vass, S. Wilczek, T. Lafleur, R. P. Brinkmann, Z. Donkó, and J. Schulze, *Plasma Sources Science and Technology* **29**, 025019 (2020).
- 950 [132] M. Vass, S. Wilczek, T. Lafleur, R. P. Brinkmann, Z. Donkó, and J. Schulze, *Plasma Sources Science and Technology* **29**, 085014 (2020).
- 951 [133] S. J. You, S. S. Kim, and H. Y. Chang, *Applied Physics Letters* **85**, 4872 (2004).
- 952 [134] S. J. You and H. Y. Chang, *Physics of Plasmas* **13**, 043503 (2006).
- 953 [135] J. A. Thornton, *Journal of Vacuum Science and Technology* **15**, 171 (1978).
- 954 [136] A. V. Phelps and Z. L. Petrovic, *Plasma Sources Science and Technology* **8**, R21 (1999).
- 955 [137] M. Daksha, A. Derzsi, S. Wilczek, J. Trieschmann, T. Mussenbrock, P. Awakowicz, Z. Donkó, and J. Schulze, *Plasma Sources Science and Technology* **26**, 085006 (2017).
- 956 [138] Y. Fu, B. Zheng, D.-Q. Wen, P. Zhang, Q. H. Fan, and J. P. Verboncoeur, *Plasma Sources Science and Technology* **29**, 09LT01 (2020).